

Numerical Simulation of Viscous Transonic Flows over an Airfoil

S.A. Velichko and Yu.B. Lifshitz

Central Aerohydrodynamic Institute, Zhukovski, Russia

Communicated by A.I. Ruban

Received 21 April 1993 and accepted 1 August 1993

Abstract. High Reynolds number viscous transonic flow is described based on an interaction of the potential outer flow with the boundary layer and wake. Following the procedure of Lighthill (1958), the solutions in these domains are matched to each other through boundary conditions. The solution to the complete problem is obtained iteratively through successive computations of the flows in the outer and inner domains. Both old and new algorithms are used for the iteration process and subsequent problem solution. Results are given for all the airfoils from the Experimental Data Base for Computer Program Assessment (AGARD-AR-138, 1979). A comparison of these results with experimental data shows the degree of agreement between these unbounded airfoil flow simulations and real transonic flow over the central part of a straight wing.

1. Introduction

The Navier–Stokes equations provide the mathematical description for viscous gas flow. However, the numerical solution of these problems is limited by the available computing capacity. This is confirmed from an analysis of airfoil flow calculations, obtained using 16 different Navier–Stokes methods and collected in Holst (1987). In flows with well-known properties, to which the flow over an airfoil belongs, the simpler mathematical models are more advantageous. An airfoil flow simulation based on the interaction of inviscid potential flow with viscous boundary-layer and wake flow is sufficient at large Reynolds number and transonic velocities. Among five codes of this type from Holst (1987), the code GRUMFOIL (Melnik *et al.*, 1987) is the leader.

In this method the velocity field has a potential which obeys the continuity equation. The normal velocity on the body is nonzero and is calculated by variations of displacement thickness and tangential velocity. The same condition is fulfilled at the streamline leaving the body, where a jump of the tangential velocity is also specified due to the curvature of this streamline. It is too difficult to construct a robust iteration method matching the solutions in the outer domain with the boundary layer and wake. A semi-inverse method is commonly used for this purpose in which the displacement thickness is specified at every iteration, and the direct problem is solved in the outer domain and the inverse in the boundary layer. The difference in pressure on the body obtained in these methods is used to update the displacement thickness by relaxation (Carter, 1979; Le Balleur, 1981).

This method is good enough only in the case of a flow that is far from separation. If the separation occurs in the aft of the airfoil, or at the intersection of the shock wave with the boundary layer, then the relaxation factor decreases and the number of iterations required to obtain a reasonable result increases significantly. Another method for the construction of a viscous–inviscid interaction, which is free from the limitations of the semi-inverse one, was proposed by Velichko (1990). It is used here for

the numerical simulation of transonic flow over an airfoil. A comparison of the computed results with experimental data shows the degree of correlation between the mathematical model and the real flow.

2. Viscous-Inviscid Interaction

At high Reynolds numbers the effect of viscosity is confined to a narrow region near the body and wake. Outside of this domain, the ratio of friction forces to inertial ones is the reciprocal of the Reynolds number, and hence the viscosity can be neglected, and a potential flows exists. In the boundary layer and wake, which are thin layers, the flow satisfies the Prandtl equations. On the body surface the velocity components and heat flux are zero. The potential approximation in transonic flow theory is based on the assumption that the resulting shock waves are weak. If this assumption holds, the entropy variation in the shocks, which is of the order of the third power of their intensity, is neglected, and the entropy is taken as a constant in the whole flow region:

$$S = S_\infty. \quad (1)$$

Accordingly, the potential approximation is satisfied by the leading term of an expansion of the Euler equations solution in the small parameter $\varepsilon = \max(M_\perp - 1)$, where M_\perp is the Mach number before the shock, and the maximum is sought over the entire flow region.

From the normal streamline momentum equation, which is known as the Crocco equation, the velocity field for isentropic flow has a potential

$$\mathbf{q} = \text{grad } \Phi. \quad (2)$$

The potential Φ is determined from the continuity equation, in which the velocity derivatives satisfy

$$\text{div}(\rho \text{ grad } \Phi) = 0, \quad (3)$$

and the density ρ is a function of the velocity modulus q :

$$\rho = \left[1 + \frac{\kappa - 1}{2} M_\infty^2 (1 - q^2) \right]^{1/(\kappa - 1)}, \quad (4)$$

where κ is the Poisson adiabatic exponent, and M_∞ is the Mach number at infinity. The density ρ and the velocity q are scaled by their freestream values, and the unit of length is the airfoil chord.

Because the density ρ in (3) is a function of the potential derivatives, this equation is nonlinear and is of a mixed elliptic-hyperbolic type: elliptic at subsonic and hyperbolic at supersonic velocities. In the supersonic region, (3) admits solutions with surfaces of discontinuity of the potential derivatives, which represent the shock waves of real supersonic flows. Other relations must be satisfied at these surfaces instead of the exact Rankine-Hugoniot conditions at the shocks. These exact relations cannot be applied in our approximation because the isentropic equation (1) is in contradiction with the conditions of conservation mass, momentum, and energy at the shock front.

Only two relations between the velocity components can be taken at the shock in (3) and (4) for the potential. One of them is continuity of the tangential velocity, which leads to continuity of the potential across the shock wave:

$$[\Phi] = 0. \quad (5)$$

The integral counterpart of (3) is commonly used as the second relation, which means that the mass flow from the viewpoint of (4) for the density is continuous across the shock.

These conditions are very hardy in computations because they are satisfied automatically when (3) is approximated by any conservative scheme. However, they lead to an error of $O((M_\perp - 1)^2)$ even in the case of a uniform flow with a shock wave. While the potential character of the velocity field does not break down in this case, an error of $O((M_\perp - 1)^3)$ due to (1) gives rise to a greater error in postshock velocities. It is clear that the second condition is responsible for this error transformation. We can avoid it by replacing this condition by the Prandtl-Meyer relation between velocity components at the front of an oblique shock,

$$q_{1n} q_{2n} = \frac{2}{\kappa + 1} M_\infty^{-2} + \frac{\kappa - 1}{\kappa + 1} (1 - q_\tau^2), \quad (6)$$

which is a direct corollary of the Rankine–Hugoniot conditions. Here the subscripts 1 and 2 refer to the normal velocity at the different shock surfaces. The numerical implementation of condition (6) is carried out by source distributions along the shock front:

$$\sigma = \rho_1 q_{1n} \left\{ \left[\frac{2\kappa M_{1n}^2 - \kappa + 1}{\kappa + 1} \right]^{1/(\kappa-1)} \left[\frac{(\kappa-1)M_{1n}^2 + 2}{(\kappa+1)M_{1n}^2} \right]^{\kappa/(\kappa-1)} - 1 \right\}.$$

The modified potential approximation (Lifshitz and Shagaev, 1989) with conditions (5) and (6) and the Euler equations give identical postshock velocities in the problems with straight or oblique shock waves, even though the density and pressure in them differ by $O(\varepsilon^3)$. The computation of transonic airfoil flows show that this approximation correlates well with the Euler equations in a wider domain than the standard one and overlaps the flight velocity range of a subsonic airplane.

The velocity components must be matched at the boundary of the viscous and inviscid flows. For the outer flow, this boundary is moved to the body surface and streamline leaving its trailing edge, as in boundary-layer theory. This is a principal proposition of the viscous–inviscid interaction theory (Lighthill, 1958), which enables the boundary condition on the airfoil to be written as a relation between the potential derivatives:

$$\rho \frac{\partial \Phi}{\partial n} = \frac{\partial}{\partial s} \left(\rho \delta^* \frac{\partial \Phi}{\partial s} \right). \quad (7)$$

The boundary conditions are also set on the streamline leaving the airfoil trailing edge:

$$\langle \rho \rangle \left[\frac{\partial \Phi}{\partial n} \right] = \frac{\partial}{\partial s} \left\langle \rho \delta^* \frac{\partial \Phi}{\partial s} \right\rangle, \quad \left[\frac{\partial \Phi}{\partial s} \right] = - \left\langle \frac{\partial \Phi}{\partial s} \right\rangle k(s) (\delta^* + \theta). \quad (8)$$

Here, s and n are the coordinates along the normal to the airfoil and wake, $k(s)$ is the wake curvature, δ^* and θ are the displacement thickness and the momentum thickness, $[]$ denotes the difference of values at the streamline edges, and $\langle \rangle$ denotes their average.

The boundary-value problem for the potential is augmented by the condition at infinity:

$$\text{grad } \Phi = \mathbf{q}_\infty. \quad (9)$$

The displacement thickness δ^* and the momentum thickness θ , in conditions (7) and (8), are obtained from the Prandtl equation for the boundary layer and wake. The velocity $u_e(s)$ at the outer boundaries of these layers is equal to $\partial \Phi / \partial s$ from the outer problem on the airfoil surface and streamline leaving its trailing edge.

3. Computation of the Potential

A simplified version of the problem formulated in (2)–(9) is solved. Simplification is obtained by setting the first of relations (8) along the grid line passing through the airfoil trailing edge, and replacing the second of them by the Kutta–Zhukovski condition, which is its inviscid counterpart. This modification simplifies the algorithm significantly, and, in accordance with Melnik *et al.* (1977), does not lead to a noticeable error for cases of moderate lift. Moreover, attempts to satisfy the second of relations (8) can become a source of error because the right-hand side of this equation decreases rapidly when going away from the trailing edge, and correct calculations at the trailing edge are difficult due to the singularity at this point (Velichko and Lifshitz, 1990).

The solution of the viscous–inviscid problem is obtained by successive iterations. The potential problem is solved by iterations as well. The boundary conditions (7) and (8) are modified to speed up the convergence of the inner and global iterations. More complicated relations given by

$$R \frac{\partial \Phi}{\partial n} = G \frac{\partial^2 \Phi}{\partial s^2} + T \frac{\partial \Phi}{\partial s} + F, \quad R \left[\frac{\partial \Phi}{\partial n} \right] = G \frac{\partial^2 \Phi}{\partial s^2} + T \frac{\partial \Phi}{\partial s} + F, \quad (10)$$

have to be satisfied instead of (7) and (8), in which R , G , T , and F are the known functions of s , and R and G are of the opposite sign.

Equations (2)–(6), (9), and (10) are computed by the mesh-projection method, which has been published (Lifshitz and Shagaev, 1988) for the standard potential approximation and boundary

condition (10) with zero on the right-hand sides. The Karman–Trefftz transformation and the Garrick–Theodorsen (Theodorsen and Garrick, 1933) iterations are used for grid generation by a conformal mapping of the airfoil to the circle. An additional compression of the grid to the airfoil image, and its leading and trailing edges, increases the accuracy of the flow computations and gives good results on a relatively coarse grid of 127×28 nodes. The Cartesian coordinates of the nodes correspond to the nodes of a uniform rectangular grid $\Omega_h(\xi, \eta)$ in the computational domain. This allows the introduction of the coordinate transformation

$$x = x(\xi, \eta), \quad y = y(\xi, \eta),$$

which is bilinear inside each mesh and serves to compute the Jacobian J and metric coefficients A , B , and C :

$$J = (x_\xi y_\eta - x_\eta y_\xi)^{-1}, \quad A = J^2(x_\eta^2 + y_\eta^2), \quad B = -J^2(x_\xi x_\eta + y_\eta y_\xi), \quad C = J^2(x_\xi^2 + y_\xi^2).$$

In the domain $\Omega(\xi, \eta)$, the continuity equation (3) for the velocity potential $\Phi(\xi, \eta)$ can be written in the form

$$\frac{\partial}{\partial \xi} \left(\rho \frac{U}{J} \right) + \frac{\partial}{\partial \eta} \left(\rho \frac{V}{J} \right) = 0, \quad (11)$$

where U and V are the contravariant velocity components:

$$U = A\Phi_\xi + B\Phi_\eta, \quad V = B\Phi_\xi + C\Phi_\eta,$$

while the density is connected to the velocity modulus squared,

$$q^2 = U\Phi_\xi + V\Phi_\eta,$$

by Bernoulli's equation (4).

The bottom $\eta = \eta_1$ of the rectangular domain $\Omega(\xi, \eta)$ corresponds to the airfoil surface, the top $\eta = \eta_K$ to the external boundary of the flow domain, and the lateral sides $\xi = \xi_1$ and $\xi = \xi_I$ to the edges of the cut made from the airfoil trailing edge to the external boundary. Condition (10) on the line $\eta = \eta_1$ is written as

$$R \frac{V}{J} = G \frac{\partial}{\partial \xi} \left[(x_\xi^2 + y_\xi^2)^{-1/2} \frac{\partial \Phi}{\partial \xi} \right] + T \frac{\partial \Phi}{\partial \xi} + F(x_\xi^2 + y_\xi^2)^{1/2}. \quad (12)$$

On the lateral boundaries, the jump of the potential has a constant value Γ equal to the velocity circulation along the airfoil contour,

$$\Phi(\xi_1, \eta) - \Phi(\xi_I, \eta) = \Gamma, \quad (13)$$

and condition (10) gives the source distribution

$$\frac{R}{J} [U(\xi_1, \eta) - U(\xi_I, \eta)] = G \frac{\partial}{\partial \eta} \left[(x_\eta^2 + y_\eta^2)^{-1/2} \frac{\partial \Phi}{\partial \eta} \right] + T \frac{\partial \Phi}{\partial \eta} + F(x_\eta^2 + y_\eta^2)^{1/2}. \quad (14)$$

On the external boundary of the computational domain, the potential is given by

$$\Phi(\xi, \eta_K) = \Gamma \gamma(\xi, \eta_K) + X(\xi, \eta_K) \cos \alpha + Y(\xi, \eta_K) \sin \alpha + Qv(\xi, \eta_K). \quad (15)$$

Here, α is the angle of attack of the airfoil, while the functions γ , X , Y , and v are defined in Lifshitz and Shagaev (1988, 1989), and serve to describe the potential of the source with intensity Q and the vortex with circulation Γ located in the middle of the airfoil.

In order to discretize (11), a staggered grid of balance meshes Ω^h is introduced in addition to the rectangular grid Ω_h , with values of the potential and Cartesian coordinates placed at the nodes. The nodes of this grid are in the middle of the Ω_h meshes. The grid counterpart of (11) results from integration of this equation over all the balance meshes and replacement of the area integrals by integrals over the boundaries

$$\oint_{\partial \Omega^h} \bar{\rho} \frac{U}{J} d\eta - \bar{\rho} \frac{V}{J} d\xi = r. \quad (16)$$

Here, according to (6), r is not equal to zero only in the case of a shock in the balance mesh, while $\bar{\rho}$ and $\tilde{\rho}$ are modified densities. They replace the standard density ρ in the supersonic domains to obtain a stable solution and are equal to the mass flow ρq shifted upstream in ξ or η and divided by q in the mesh under consideration.

In order to transform (16) into a system of equations for the potential values at the grid nodes, Φ and the Cartesian coordinates x, y inside the meshes are computed by a bilinear isoparametric representation, while the density is assumed to be a constant in each mesh and is equal to the value at its center. The integrals in (16) are evaluated by composite quadrature formulas with one node in each mesh. The resulting grid equations are consistent with uniform flow and in the case of $\rho = 1$, $x = \xi$, and $y = \eta$, when (11) transforms to the Laplace equation, they are identical with the standard form of the five-point scheme on a stencil of the "cross" type.

On the side $\eta = \eta_1$ of the balance meshes, the mass flow is given by (12). To avoid a division by R , which can be zero, (16) is multiplied by R , and then RV/J is substituted according to (12). A similar procedure is applied in the evaluation of the integrals of (16) over the balance meshes at the lateral sides of Ω_h . In this case the integral of the source distribution on the grid line passing through the airfoil trailing edge is calculated according to the boundary condition (14). The potential on the upper edge of this line is excluded by (13). Equation (15) is used to obtain the mesh equations at the outer boundary of the domain Ω_h . The Kutta–Zhukovski condition which expresses the equality of flow velocities on the upper and lower airfoil surfaces at its trailing edge completes the mesh equation system.

A solution to this system of nonlinear equations is achieved through an iterative procedure. The linear equations for the correction are obtained when the density is taken from the previous iteration and then solved by a multigrid algorithm with red–black block overrelaxation as a smoother. The Kutta–Zhukovski condition is implemented on the finest grid only, and the correction $\Delta\Gamma$ is used to add $\Delta\Gamma\gamma(\xi, \eta)$ to the potential at all the grid nodes. At the end of the iteration, the new source distribution on the shock front is computed, and $\Delta Qv(\xi, \eta)$ is added to the potential Φ .

4. Boundary Layer

Laminar boundary-layer calculations, initiated at the leading-edge stagnation point, are carried out by using an integral relations method (Bossel, 1971). A sudden transition to turbulent flow at a position along the surface can be either prescribed or determined from Michel's transition criteria (Cebeci and Smith, 1974). The code also tests for leading-edge bubble separation and sets the transition point at the location of laminar separation if one arises during the computation.

The solution for the turbulent boundary layer is based on a generalization of Green's lag entrainment method. As in the original method (Green *et al.*, 1977), a momentum integral equation is used,

$$\frac{d}{ds}(\rho_e u_e^2 \theta) + \rho_e u_e \delta^* \frac{du_e}{ds} = \frac{1}{2} C_f \rho_e u_e^2, \quad (17)$$

and an equation for the mass variation in the boundary layer with entrainment coefficient C_E ,

$$\frac{d}{ds}[\rho_e u_e (\delta - \delta^*)] = \rho_e u_e C_E. \quad (18)$$

The turbulent kinetic energy at the point of maximum stress serves to determine C_E :

$$\frac{dC_E}{ds} = \frac{2}{\theta} \frac{C_\tau}{\partial C_\tau / \partial C_E} \left\{ a_1 \frac{u_e}{u_m} \frac{\delta}{L} (C_{\tau EQ}^{1/2} - \lambda C_\tau^{1/2}) \frac{\theta}{\delta} + \left[\frac{\theta}{u_e} \frac{du_e}{ds} \right]_{EQ} - \frac{\theta}{u_e} \frac{du_e}{ds} \left[1 + 0.075 M_e^2 \left(\frac{1 + 0.2 M_e^2}{1 + 0.1 M_e^2} \right) \right] \right\}, \quad (19)$$

where the subscript e denotes the outer boundary of the layer.

Green's original method was restricted to attached flow mainly because of the specific relations used for the turbulent closure. In our extension of the method to separated flow, we take the flow

velocity profile as a superposition of the law of the wall and the wake function:

$$\frac{u}{u_e} = 2.44v_* \ln \eta + S_0 + (1 - S_0) \sin^\chi \left(\frac{\pi}{2} \eta \right), \quad \eta = \frac{y}{\delta}, \quad (20)$$

in which

$$v_* = C_f \left(\frac{1 + 0.18M_e^2}{2|C_f|} \right)^{1/2}, \quad S_0 = 2.44v_*[2.09 + \ln(R_\delta v_*)],$$

and the exponent χ in the wake function

$$\chi = F \left(\frac{\theta}{u_e} \frac{du_e}{ds} - \left[\frac{\theta}{u_e} \frac{du_e}{ds} \right]_{\text{EQ}} \right),$$

is taken as in Cross (1986) and Lock (1986). This three-parameter formula enable us to incorporate a departure from equilibrium in the case of separation. The incompressible parameters δ_k^* and θ_k are computed by integration of the velocity profile. Relations between the shape factor $H = \delta^*/\theta$, displacement thickness δ^* , momentum thickness θ , and their counterparts, when $\rho = \rho_e$ (Thomas, 1984),

$$H = H_k(1 + 0.113M_e^2) + 0.290M_e^2,$$

$$\delta^* = \delta_k^* + \theta M_e^2 \left(\frac{0.064}{H_k - 0.8} + 0.251 \right),$$

are applied to calculate δ^* and θ .

Some terms on the right-hand side of (19) and in the expression for χ are obtained with the velocity profile (20), the others are evaluated by formulas from the work of Green *et al.* (1977):

$$\left(\frac{\theta}{u_e} \frac{du_e}{ds} \right)_{\text{EQ}} = \frac{1.25}{H} \left\{ \frac{C_f}{2} - \left(\frac{H_k - 1}{6.432H_k} \right)^2 (1 + 0.04M_e^2)^{-1} \right\},$$

$$C_\tau = (1 + 0.1M_e^2)(1.2C_E^2 + 0.024C_E + 0.32C_{f0}),$$

$$(1 + 0.2M_e^2)^{1/2} C_{f0} = \frac{0.01013}{\log[(1 + 0.056M_e^2)R_\theta] - 1.02} - 0.00075.$$

The entrainment coefficient at equilibrium, $(C_E)_{\text{EQ}}$, results from the elimination of $d\theta/ds$ in (17) and (18) on the assumption that Head's shape parameter $H_1 = (\delta - \delta^*)/\theta$ depends on H_k only and $dH_k/ds = 0$ is the equilibrium condition. This gives an equality

$$(C_E)_{\text{EQ}} = H_1 \left[\frac{C_f}{2} - (H + 1) \left(\frac{\theta}{u_e} \frac{du_e}{ds} \right)_{\text{EQ}} \right]. \quad (21)$$

The derivative dH_1/dH_k at large H_k is near zero and (21) becomes invalid. In this case the estimation of $(C_E)_{\text{EQ}}$ results from a definition of the entrainment coefficient:

$$C_E = \left[\frac{\partial \tau / \partial y}{\rho u_e \partial(u_e - u) / \partial y} \right]_{y=\delta}, \quad \tau = \rho K_1 y^2 \left| \frac{\partial u}{\partial y} \right| \frac{\partial u}{\partial y}.$$

Substituting the velocity profile (20) with $\chi = 2$, $K_1 = 0.08$ (Green *et al.*, 1977), and neglecting v_* relative to unity, we obtain $(C_E)_{\text{EQ}} = 0.063$, which replaces the value determine from (21) after this value has been reached. As in Green's original method, a structure function is set to $a_1 = 0.15$, a dissipation length scale is taken as $L = 0.08\delta$, but a velocity ratio $(u_e/u_m) = 1.5$ at $H_k \leq 2$ is changed to $3H_k/(2 + H_k)$ at $H_k > 2$ according to Thomas (1984). A coefficient λ , incorporating secondary factors, equals 1 in the boundary layer and $\frac{1}{2}$ in the wake.

Initial data for the turbulent boundary-layer computation are specified at the transition point. At this point, θ is assumed to be continuous, the Dvorak and Woodward (1977) method, taking into account intermittency, is used for the δ^* evaluation, and C_E results from the condition that the right-hand side of (19) is zero. The wake flow is also described by (17), (18), and (19), in which $C_f = C_{f0} = 0$. In this case the term with the law of the wall is absent in the velocity profile (20), S_0 becomes a unknown function instead of v_* , and the initial data are taken at the airfoil trailing edge.

The displacement thickness and momentum thickness are continuous at this point, and C_E is specified as its equilibrium value.

In the standard application of the lag entrainment method, the functions θ , H_k , and C_E are unknown, the velocity profile is not specified, and some generalization of experimental data serves as closure conditions. When the direct problem is solved by this method at $H_k \geq 3$, the error becomes too large. It can be avoided if the inverse problem is solved. This is because the unknown function $H_1(\theta, H_k, \dots)$ is replaced by a simple closure condition $H_1(H_k)$. Because the derivative $dH_1/dH_k \ll 1$ at $H_k \geq 3$, the system of linear equations (17)–(19) for the derivatives of the unknown functions becomes ill conditioned and results in a drastic rise in the error. In the present generalization of the method, the unknown functions are v_* , δ , and C_E , but the integral characteristics and shape factors result from an evaluation of the integrals and recalculation with compressible formulas. This procedure yields a decrease in the error in the boundary-layer and wake computations.

Generally speaking, a solution to the initial value problem (17)–(19) does not exist at every given velocity distribution $u_e(s)$. This means that at some value of the independent variable s_0 , this system cannot be solved relative to the derivatives given on the right-hand side, although it might be solved if some additional relation is specified. Therefore, this system cannot be employed as a part of the iteration method and ought to be changed to another, which has a solution at any $u_e(s)$ arising during

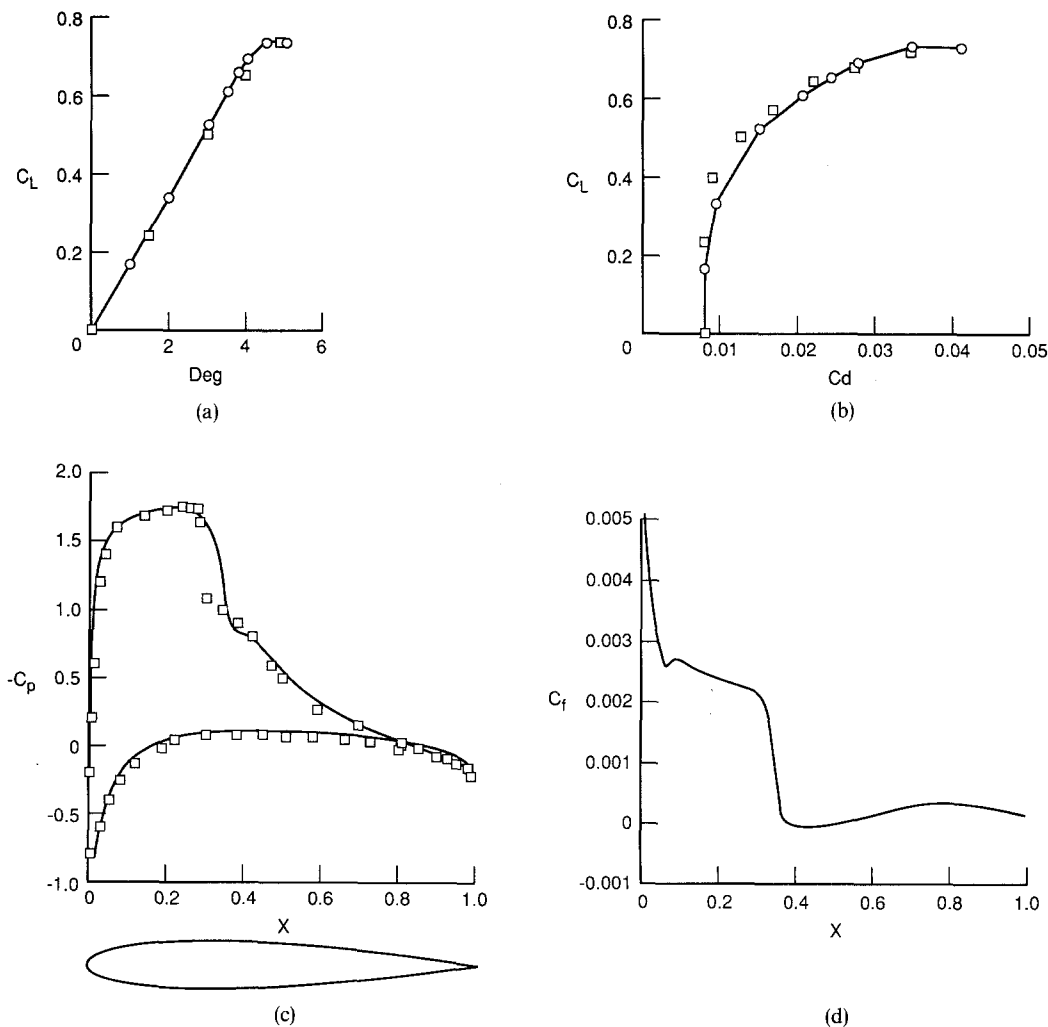


Figure 1. Comparison of computed and experimental (\square , Harris) data for the NACA-0012 airfoil at $M_\infty = 0.7$ and $Re = 9 \times 10^6$. (a) Lift versus angle of attack, (b) lift versus drag polar, (c) pressure coefficient at $\alpha = 5^\circ$, (d) skin friction coefficient distribution on upper surface at $\alpha = 5^\circ$.

the iterations. In order for such a problem to be constructed, we use the boundary condition (7) in the form of

$$\frac{d}{ds}(\rho_e u_e \delta^*) = \rho_e v_e \quad (22)$$

and make a system of two equations, which are a linear combination of (17), (18), and (22). These are used instead of the integral momentum and mass equations. The system that is solved at any $u_e(s)$ and $v_e(s)$ can be selected from this two-parameter family. They are coupled with (19) for the boundary-layer and wake computations during the iterations, and are solved by a second-order Euler method.

As is shown in Le Balleur (1981), the boundary-value problem (10), which has to be solved for the calculation of the viscous-inviscid interaction, is unstable if $R(s)$ and $G(s)$ have the same sign. This special feature precludes employing boundary condition (7) in the original form and calls for its modification during the iterations. Here, we use (17) and (18) to modify this condition and obtain a well-posed problem in the form of (10) that can be adequately solved by our multigrid method.

5. Comparison of Computed Results

The main source of experimental data, used here for comparison, are the measured flow parameters on straight wings, with unchanged cross sections along their span, and collected in the Experimental Data Base for Computer Program Assessment (AGARD-AR-138, 1979) for checking computational fluid dynamic methods. The wing is placed between the side walls of a wind-tunnel test section. The flow over the wing can be considered two-dimensional if the actions of wing deformation (spanwise variation), the boundary layer on the side walls, the slots on the top and bottom walls of the wind tunnel, etc., are neglected. Transition of the airfoil boundary layer is mainly defined by the pressure distribution and Reynolds number, but the level of turbulence of the wind-tunnel flow, roughness of the body surface, and pressure holes, which are not taken into account in the numerical model, act on this position as well.

The wind-tunnel walls affect the far-field flow which leads to an appreciable difference in the angle of attack of the airfoils in the wind tunnel compared with free air at the same lift. At transonic

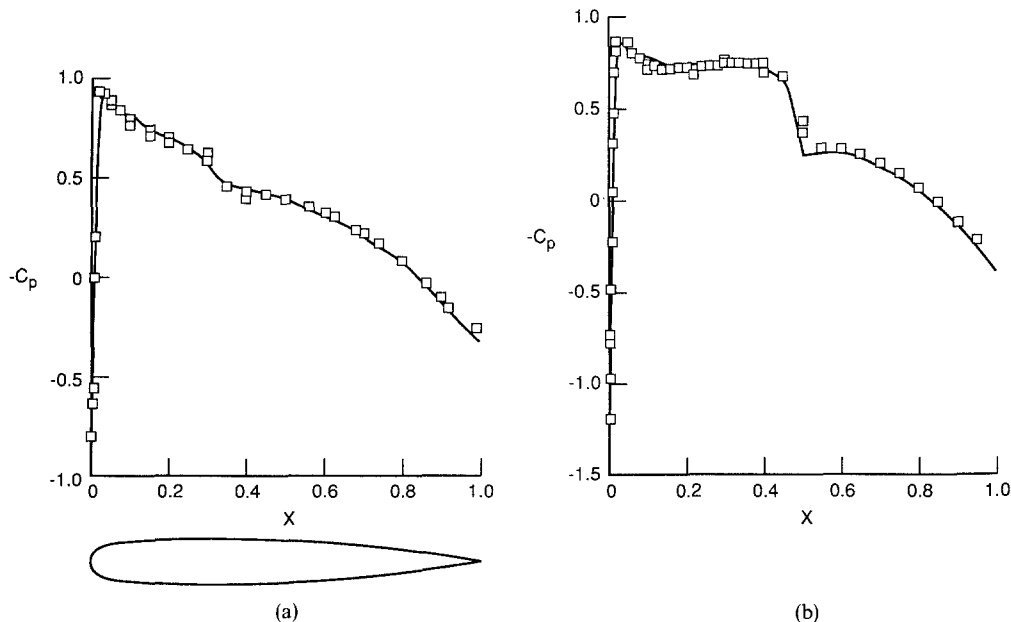


Figure 2. Comparison of computed and experimental pressure coefficient distributions for the NLR QE 0.11-0.75-1.375 airfoil at $\alpha = 0$. (a) —, Calculation: $M_\infty = 0.79$ and $Re = 2.31 \times 10^6$; \square , experiment: $M_\infty = 0.80$ and $Re = 2.31 \times 10^6$. (b) —, Calculation: $M_\infty = 0.810$ and $Re = 23.1 \times 10^6$; \square , experiment: $M_\infty = 0.815$ and $Re = 23.1 \times 10^6$.

velocities, blockage comes into play decreasing the Mach number of the flow at infinity. Therefore, full agreement between the airfoil pressure distributions in wind-tunnel tests and free-air computations should not be expected. In order to judge the consistency of the numerical simulation and experimental data, it is enough to have a correlation between lift-to-drag polars, values of C_L at which the function $C_L(\alpha)$ departs from a linear one, and an airfoil pressure coefficient distribution $C_p(x)$ at appropriate C_L and M in the far field.

NACA 0012 Airfoil

This 12%-thick symmetrical airfoil is widely used for testing different computing methods. The data on the flow over the airfoil are obtained in several wind tunnels, but, according to Holst (1987), it is best to take the data from Harris's tests in the Langley 8-Foot Transonic Pressure Tunnel (Harris,

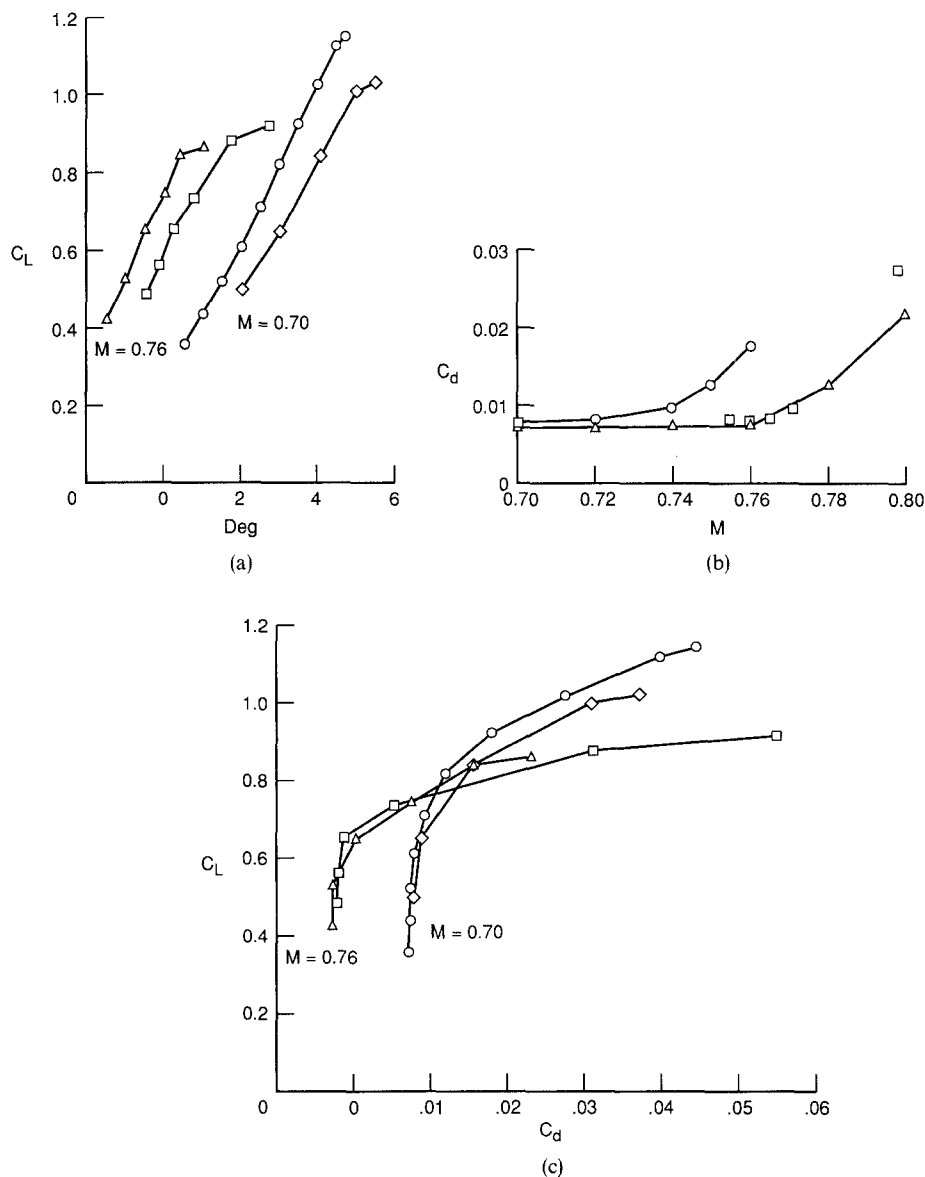


Figure 3. Comparison of computed and experimental aerodynamic coefficients for the MBB-A3 airfoil at $Re = 6 \times 10^6$. (a) Lift versus angle of attack at $M_\infty = 0.76$ and $M_\infty = 0.70$: Δ , \circ , calculation; \square , \diamond , experiment. (b) Drag versus Mach number at $\alpha = 1^\circ$ and $\alpha = 2^\circ$: Δ ($\alpha = 1^\circ$), \circ ($\alpha = 2^\circ$), calculation; \square ($\alpha = 1.89^\circ$) experiment. (c) Lift versus drag polar at $M_\infty = 0.76$ and $M_\infty = 0.70$: Δ , \circ , calculation; \square , \diamond , experiment.

1981). In the present work, however, we have taken the data from Holst (1987) and Haase *et al.* (1987), where the Harris data is partially given.

Computations were performed at a Reynolds number of $Re = 9 \times 10^6$ with the transition point fixed at 5% chord on both the upper and lower surfaces of the airfoil. Comparison of the computed results with Harris's data are shown in Figure 1 at $M_\infty = 0.7$ and different angles of attack. Good agreement with the lift coefficient at given α is obtained by correction of α and C_L for wall interference according to Harris's estimates, while the drag polar matching indicates that our numerical solution describes the real airfoil transonic flow adequately. The pressure coefficient distribution at $\alpha = 5^\circ$ agrees well with experimental data at $C_L = 0.737$. The distribution of the skin-friction coefficient shows the shock-induced separation, which occurred in the flow, reattaches downstream. This flow is typical near a buffet boundary, and Navier–Stokes computations made at $\alpha = 6^\circ$ and 7° (Maksymiuk and Pulliam, 1987) only give an unsteady periodic flow.

NLR QE 0.11-0.75-1.376 Airfoil

This 11.7%-thick symmetrical airfoil with a “peaky” pressure distribution was designed by a hodograph method (Nieuwland, 1967) as shock free at $M_\infty = 0.786$ and $\alpha = 0$. The tests performed for the experimental verification of such a flow were very accurate. The zero angle of attack excluded the source of most of the differences between wind-tunnel and free-air flows due to a lift force. The tests were carried out at a moderate Reynolds number (2×10^6) in the NLR Pilot Wind Tunnel and at $Re = 20 \times 10^6$ in the two-dimensional inset of the NAE 5 × 5-Foot Transonic Tunnel. The top and bottom walls of the NLR tunnel had a slot perforation, the ratio of its height and width to the wing chord were 3.1 and 2.3, respectively; the top and bottom walls of the NAE tunnel had a hole perforation and the above ratios were 6 and 1.5, respectively.

The pressure distributions, computed at $\alpha = 0$, free transition, and the same Reynolds number as in the tests, are compared with the test data in Figure 2. The comparison shows that the computed results correlate well with experiment if M_∞ in the computations is taken slightly less than in the tests:

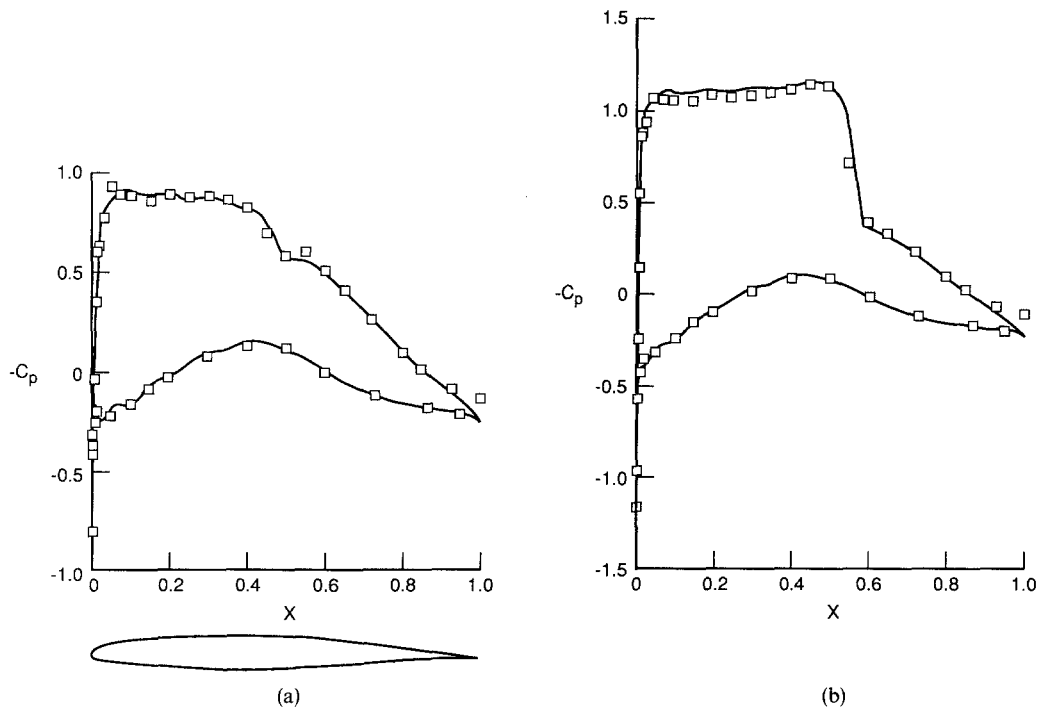


Figure 4. Comparison of computed and experimental pressure coefficient distributions for the MBB-A3 airfoil at $Re = 6 \times 10^6$. (a) —, Calculation: $M_\infty = 0.75$ and $\alpha = 1.20^\circ$; \square , experiment: $M_\infty = 0.76$ and $\alpha = 1.89^\circ$. (b) —, Calculation: $M_\infty = 0.75$ and $\alpha = 2.00^\circ$; \square , experiment: $M_\infty = 0.76$ and $\alpha = 2.75^\circ$.

by 0.01 for the NLR tunnel and by 0.005 for the NAE tunnel. However, the numerical model itself is valid for simulation of those supercritical flows at design and near-design conditions.

MBB-A3 Airfoil

The thinnest (8.9% thick) supercritical airfoil in the Experimental Data Base for Computer Program Assessment (AGARD-AR-138, 1979) was designed for a shock-free flow with $C_L = 0.58$ at $M_\infty = 0.76$ and $\alpha = 1.3^\circ$. It was tested at different Reynolds numbers: $Re = 0.4 \times 10^6$ in the wind tunnel at the Polytechnical Institute of Turin and at $Re = 6 \times 10^6$ in the ARA Bedford tunnel, whose data are used below for comparison. This tunnel had a $0.457 \text{ m} \times 0.203 \text{ m}$ rectangular test section and slot 3.2% perforation on the top and bottom walls. The chord of the straight wing was 0.127 m. The airfoil flow

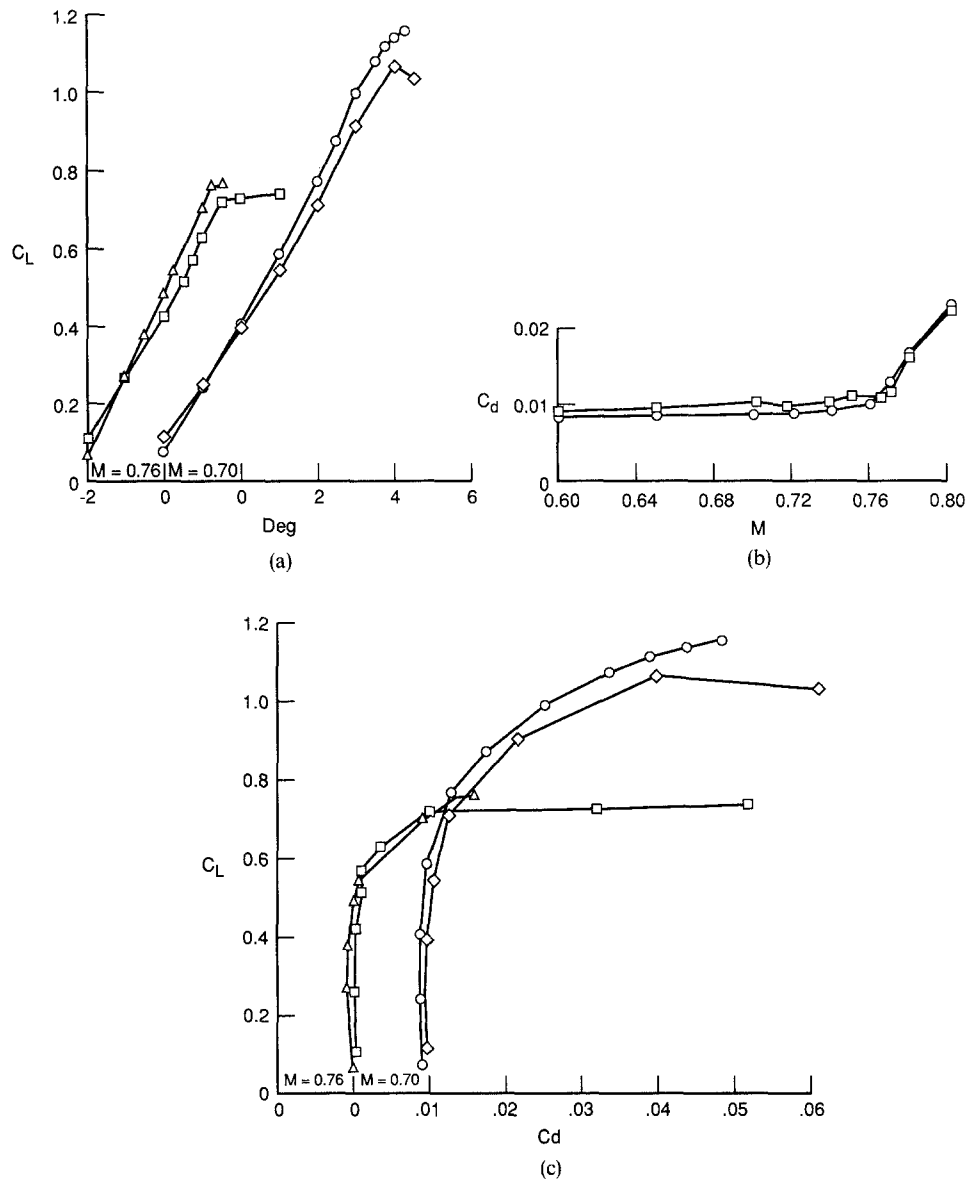


Figure 5. Comparison of computed and experimental aerodynamic coefficients for the CAST-7 airfoil at $Re = 6 \times 10^6$. (a) lift versus angle of attack at $M_\infty = 0.76$ and $M_\infty = 0.70$: Δ , \circ , calculation; \square , \diamond , experiment. (b) Drag versus Mach number: \circ ($\alpha = 0.15^\circ$), calculation; \square ($\alpha = 0.50^\circ$) experiment. (c) Lift versus drag polar at $M_\infty = 0.76$ and $M_\infty = 0.70$: Δ , \circ , calculation; \square , \diamond , experiment.

computations were performed at $Re = 6 \times 10^6$ with the transition point fixed at 30% chord on both the upper and lower surface of the airfoil.

Figure 3 shows the level of agreement between the aerodynamic coefficients. Part of the difference between the computed and experimental $C_L(\alpha)$ is explained by wall interference, and the rest by the shift of experimental data for angle of attack by $\Delta\alpha = -1.14C_L$. There is a difference in C_L values at which the shock-induced separation deflects $C_L(\alpha)$ from a straight line. It is about 5% at $M_\infty = 0.76$, but reaches 20% at $M_\infty = 0.7$. The computed $C_d(M_\infty)$ is in excellent agreement with test results if the comparison is carried out at the same C_L . The drag polars correlate with one another quite well. Comparison of pressure coefficient distribution is shown in Figure 4 for the two flow conditions. One of them is close to the design condition $M_\infty = 0.76$ and $\alpha = 1.89^\circ$, and the other corresponds to a flow with the shock at $M_\infty = 0.76$ and $\alpha = 2.75^\circ$. A reduction of Mach number by 0.01 and correction of angle of attack allow for a better correlation with experimental $C_p(x)$, but this procedure decreases the computed C_d and noticeably increases the disagreement between computed and experimental drag polars.

CAST-7 Airfoil

This 11.8%-thick supercritical airfoil with 0.5% base thickness was designed to obtain a shock-free rooftop pressure distribution with $C_L = 0.573$ at $M_\infty = 0.76$ and $\alpha = 0$. It was tested in the ARA Bedford tunnel and Transonic Wind Tunnel Braunschweig of the DFVLR, whose data are used for comparison. This tunnel with a $0.6 \text{ m} \times 0.34 \text{ m}$ test section had a 2.35% slot perforation at the top and bottom walls, and the wing chord was 0.2 m. The computations were performed at $Re = 6 \times 10^6$ with transition fixed at 7% chord on both the upper and lower surface of the airfoil, as in the test.

Figure 5 shows that the computed and experimental aerodynamic coefficients are in good agreement. A matching of $C_p(x)$ at design conditions in Figure 6 has been reached by decreasing M_∞ in the computation by 0.015. In the case of flow with a strong shock, we can match the shock position by not changing M_∞ , but the computed rarefaction downstream of the shock may be less than its experimental value, as is seen in Figure 6.

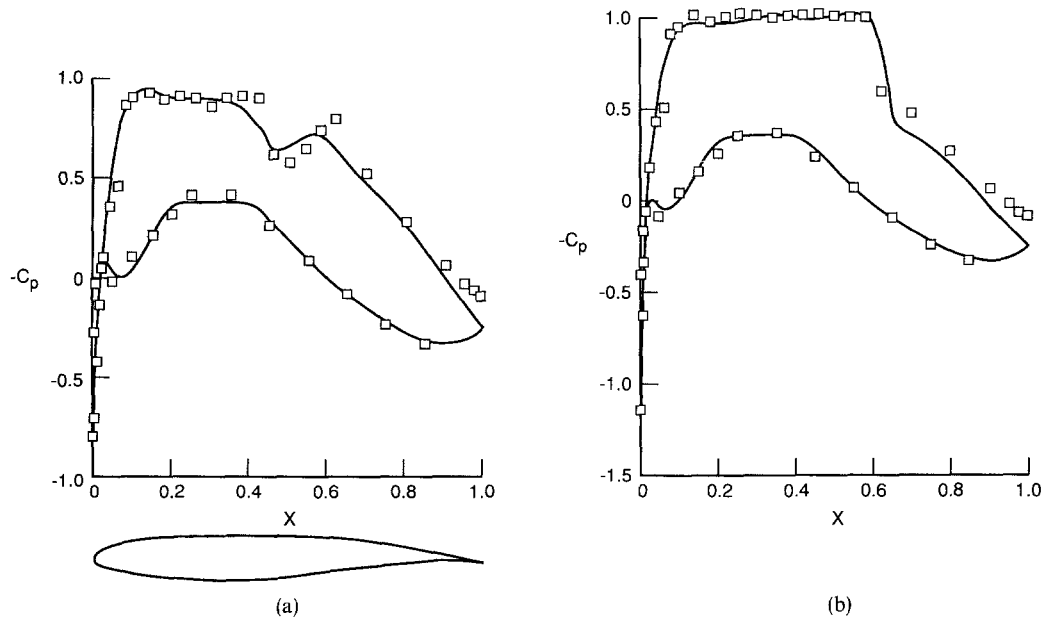


Figure 6. Comparison of computed and experimental pressure coefficient distributions for the CAST-7 airfoil at $Re = 6 \times 10^6$. (a) —, Calculation: $M_\infty = 0.745$ and $\alpha = 0.2^\circ$; \square , experiment: $M_\infty = 0.760$ and $\alpha = 0.5^\circ$. (b) —, Calculation: $M_\infty = 0.76$ and $\alpha = 0.5^\circ$; \square , experiment: $M_\infty = 0.76$ and $\alpha = 1.0^\circ$.

RAE-2822 Airfoil

A comprehensive investigation of the boundary-layer flow, which was the main part of the experimental study on this airfoil in the Experimental Data Base for Computer Program Assessment (AGARD-AR-138, 1979), was taken as the basis of two test problems by Holst (1987). The numerical solutions of these problems are presented here to find out the quality of boundary-layer simulation in the airfoil transonic flow. Figure 7 gives a comparison with experimental data at $M_\infty = 0.725$, $\alpha = 2.92^\circ$, $Re = 6.5 \times 10^6$, and a fixed transition at 3% chord. In this case good agreement is obtained not only with the pressure coefficient distribution, but with skin friction coefficient and displacement thickness as well. The flow parameters at stronger conditions ($M_\infty = 0.75$, $\alpha = 3.19^\circ$, and $Re = 6.2 \times 10^6$) are compared in Figure 8. In this case the agreement of $C_p(x)$ degrades especially downstream of the shock where the displacement thickness correlation fails. The short separation bubble, caused by the

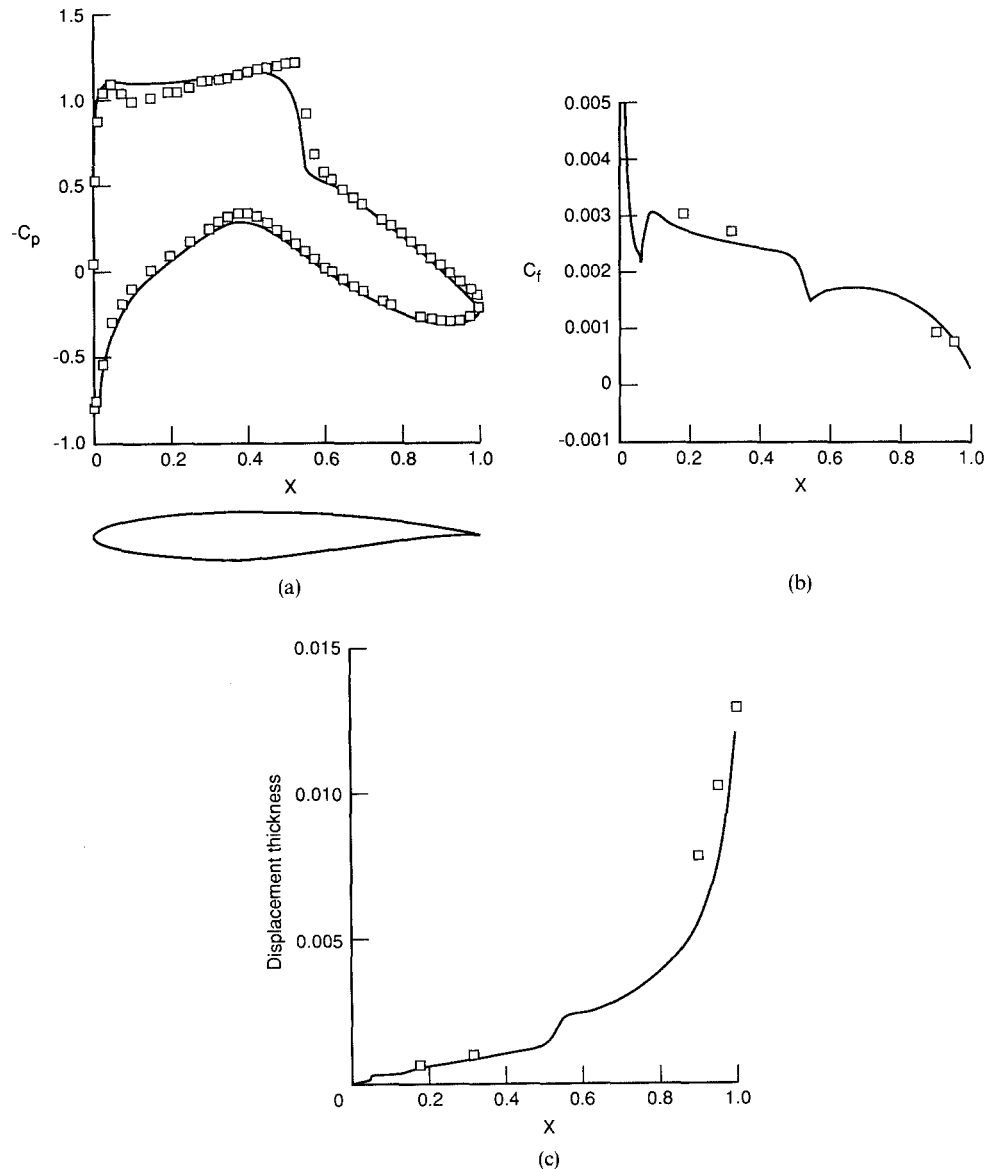


Figure 7. Comparison of computed and experimental data for the RAE-2822 airfoil at $M_\infty = 0.725$, $\alpha = 2.92^\circ$, and $Re = 6.5 \times 10^6$. (a) Pressure distributions. Calculation: $M_\infty = 0.725$ and $\alpha = 2.54^\circ$. (b) Skin friction distribution on upper surface. (c) Displacement thickness on upper surface.

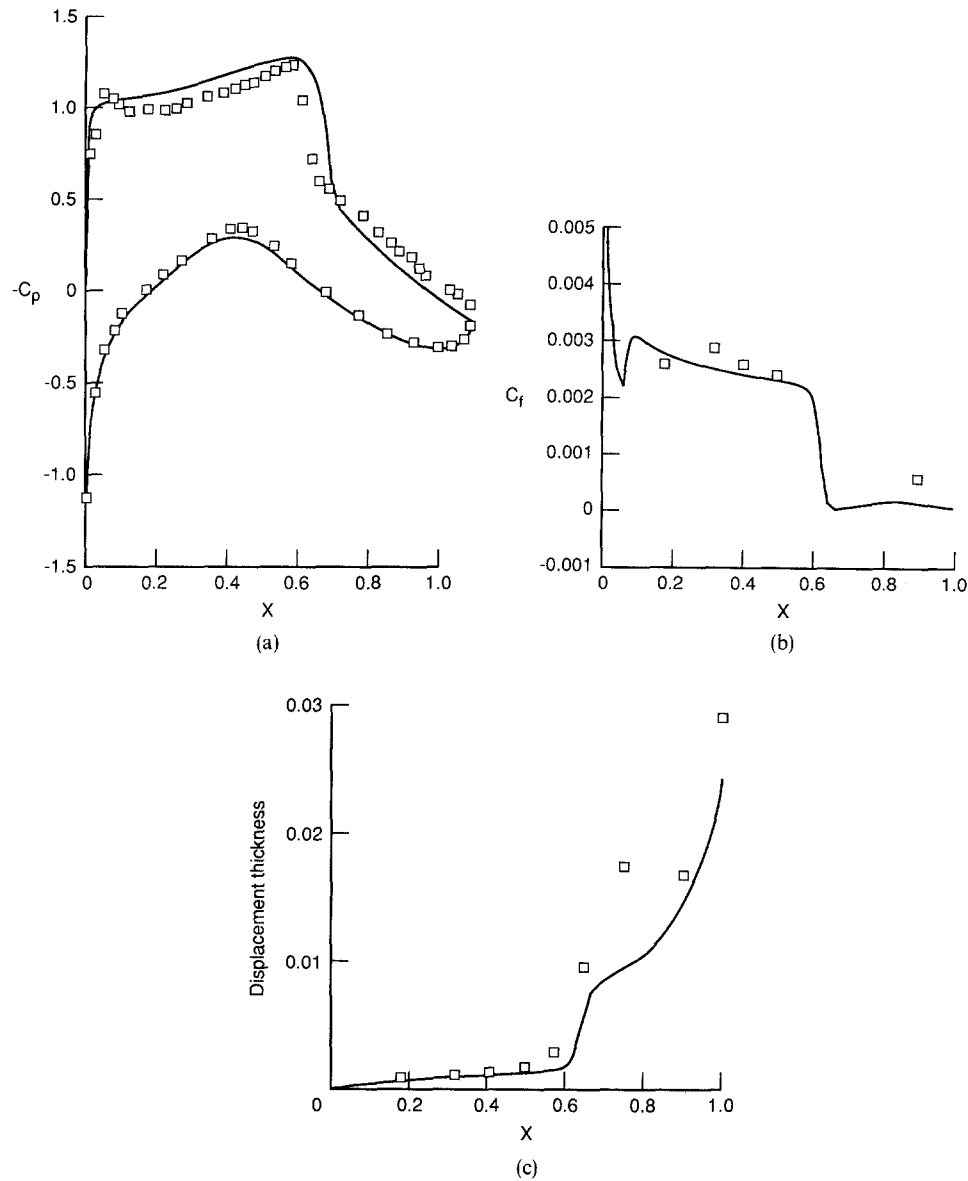


Figure 8. Comparison of computed and experimental data for the RAE-2822 airfoil at $M_\infty = 0.75$, $\alpha = 3.19^\circ$, and $Re = 6.2 \times 10^6$. (a) Pressure distributions. Calculation: $M_\infty = 0.75$ and $\alpha = 2.81^\circ$. (b) Skin friction distribution on upper surface. (c) Displacement thickness on upper surface.

shock-boundary-layer interaction and clearly shown in an oil flow test, does not appear in the computation.

NLR-7301 Airfoil

This was included in the Experimental Data Base for Computer Program Assessment (AGARD-AR-138, 1979) as the thickest (16.5% thick) supercritical airfoil. It was designed by a solution of the flow problem in a hodograph plane (Nieuwland, 1967) at $M_\infty = 0.721$ and $\alpha = 0$ when the flow is shock free and $C_L = 0.6$. The tests were carried out in the NLR Pilot Tunnel at $Re = 2.2 \times 10^6$ and both the free transition and transition were fixed at 30% chord. The experimental data at $M_\infty = 0.75$ and fixed transition show that the correlation with computed aerodynamic coefficients is good. In the case of free transition a difference in the transition-point location in the numerical model and experiment does not permit the same level of agreement. A comparison of $C_p(x)$ at design condition is given in

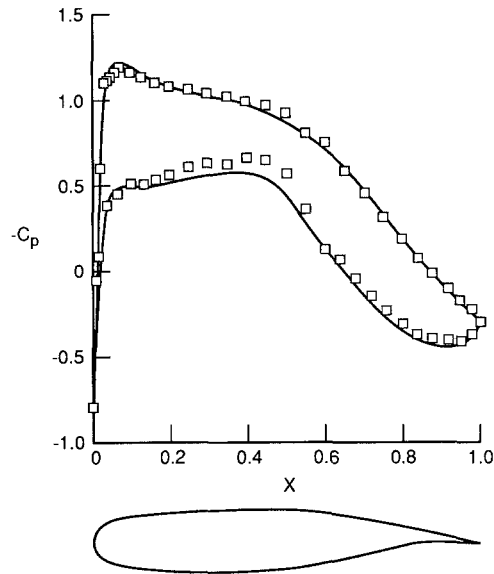


Figure 9. Comparison of computed and experimental pressure coefficient distributions for the NLR-7301 airfoil at $Re = 2.2 \times 10^6$. —, Calculation: $M_\infty = 0.725$ and $\alpha = 0^\circ$; \square , experiment: $M_\infty = 0.747$ and $\alpha = 0.215^\circ$.

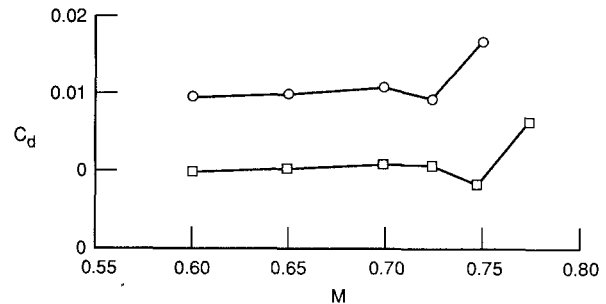


Figure 10. Drag versus Mach number comparison for the NLR-7301 airfoil at $Re = 2.2 \times 10^6$. \circ ($\alpha = -0.2^\circ$), calculation; \square ($\alpha = 0.4^\circ$), experiment.

Figure 9. A reduction of M_∞ by only 0.025 leads to agreement with experiment. This shift is clearly shown in Figure 10 where the functions $C_d(M_\infty)$ are shown at close C_L . Unfortunately, the computations with this shift in M_∞ give a drag polar which is far from the experimental one.

Supercritical NASA Airfoils

Some methods for their design and aerodynamic coefficients are given in the review by Whitcomb (1974). A part of the test results for the 10%-thick airfoil with blunt (1%) trailing edge performed in the 8-Foot Langley Pressure Tunnel are included in the Experimental Data Base for Computer Program Assessment (AGARD-AR-138, 1979). Because the code does not permit calculation of the flow over a blunted trailing edge airfoil, its aft lower surface was modified to do a sharp one. The computed results qualitatively agree with experimental data and give the correct picture for the supersonic region and shock evolution with variation of freestream conditions. However, quantitatively the functions $C_L(C_d)$ and $C_d(M_\infty)$ differ. Therefore, a comparison was made between the computed and test data for an 11%-thick airfoil with sharp trailing-edge form (Whitcomb, 1974). Calculations were carried out at a Mach number 0.01 smaller than the experiment, approximately the same lift coefficient as in the experiments, $Re = 7 \times 10^6$, and a transition fixed at 10% chord. The results for the pressure distributions are presented in Figure 11. They compare well with the experimental data in both the design and off-design cases. The skin friction distribution in Figure 11(d) points to the same boundary-layer behavior, as described by Whitcomb (1974) from oil pattern tests.

NAE-75-036-13:2 Airfoil

This is the last in the Experimental Data Base for Computer Program Assessment (AGARD-AR-138, 1979). It is 13% thick and was designed for $M_\infty = 0.75$ and $C_L = 0.36$. The tests were performed in the previously mentioned two-dimensional inset of the NAE wind tunnel at a Reynolds number $Re = 25 \times 10^6$ and free transition conditions. Calculations are carried out at the same Reynolds number and a fixed transition at 30% chord. The pressure distribution shown in Figure 12 enables the degree of agreement at design condition to be judged. In the computation a Mach number value 0.021 less than in the experiment was taken to obtain the same shock location and upstream flow as in the experiment, but still their difference downstream remains large.

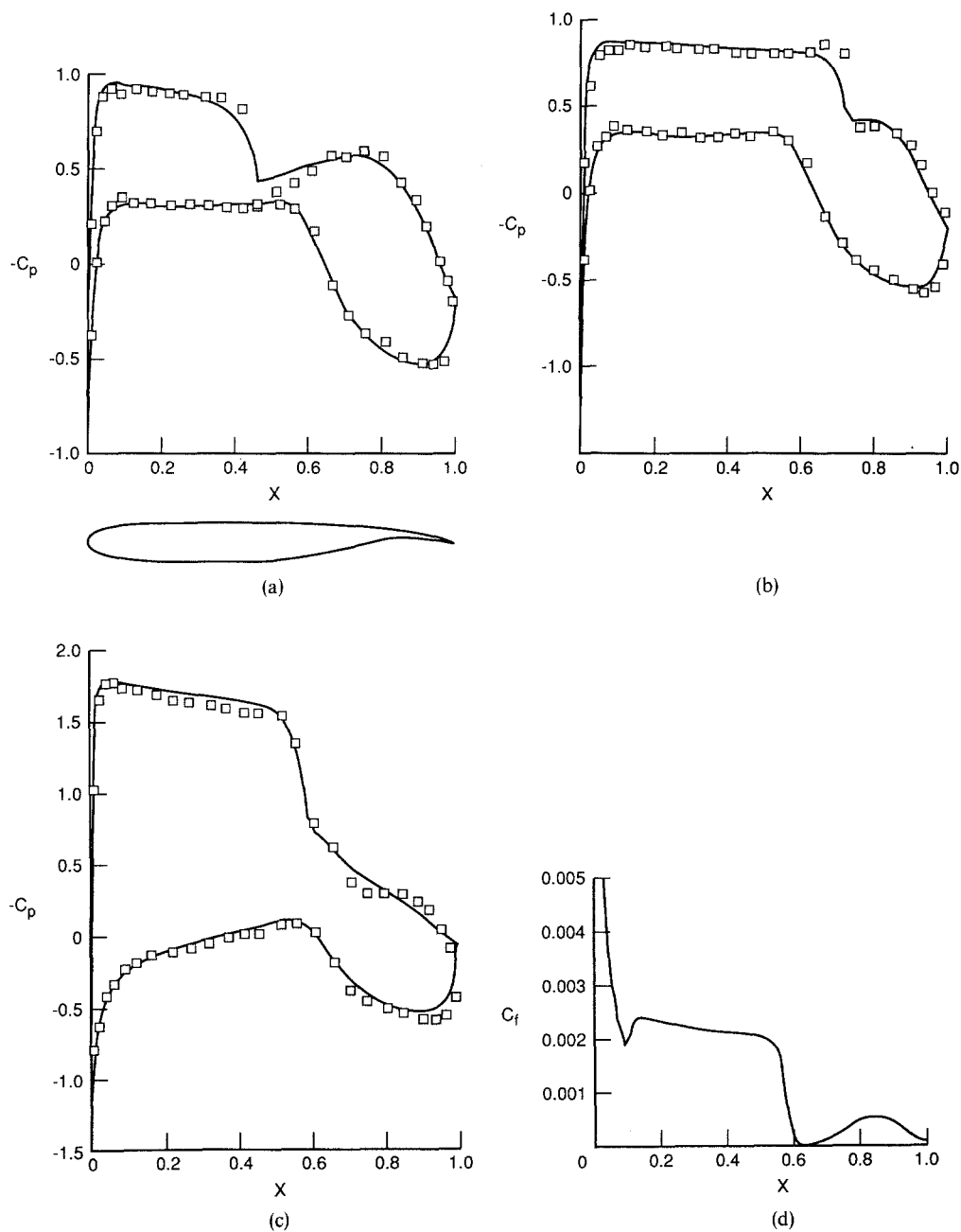


Figure 11. Comparison of computed and experimental data for the NASA 11% Supercritical airfoil at $Re = 7 \times 10^6$. (a) Pressure coefficient distributions. —, Calculation: $M_\infty = 0.77$, $\alpha = 0^\circ$, $C_L = 0.5758$, and $C_d = 0.0107$; \square , experiment: $M_\infty = 0.78$ and $C_L = 0.58$. (b) Pressure coefficient distributions. —, Calculation: $M_\infty = 0.79$, $\alpha = -1^\circ$, $C_L = 0.61$, and $C_d = 0.0117$; \square , experiment: $M_\infty = 0.80$ and $C_L = 0.61$. (c) Pressure coefficient distributions. —, Calculation: $M_\infty = 0.72$, $\alpha = 4.1^\circ$, $C_L = 1.3014$, and $C_d = 0.072$; \square , experiment: $M_\infty = 0.73$ and $C_L = 1.32$. (d) Skin friction distribution on upper surface at $M_\infty = 0.72$, $\alpha = 4.1^\circ$, $Re = 7 \times 10^6$, transition at 10% chord.

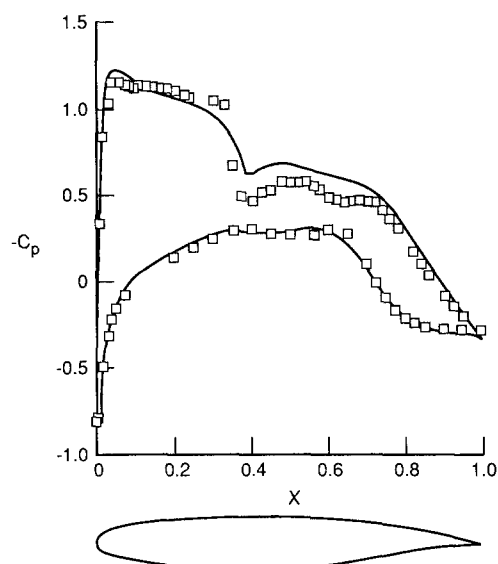


Figure 12. Comparison of computed and experimental pressure coefficient distributions for the NAE-75-036-13:2 airfoil. —, Calculation: $M_\infty = 0.73$, $\alpha = 2^\circ$, $C_L = 0.5756$, and $C_d = 0.0091$; \square , experiment: $M_\infty = 0.751$, $\alpha = 3.034^\circ$, $C_L = 0.521$, and $C_d = 0.01245$.

6. Concluding Remarks

Our comparative analysis of the flow over all the airfoils from the Experimental Data Base for Computer Program Assessment (AGARD-AR-138, 1979) implies that the proposed numerical method simulates the airfoil transonic unbounded viscous flow with the same accuracy as the wind-tunnel experiment. In the range of conditions studied the flow is steady and two-dimensional in some sense and the numerical solution is converged. The results show that this range is large enough and includes not only design regimes, but some safe limiting conditions as well.

The results also pose the question about the error arising when wind-tunnel test data are transferred to unbounded transonic flow. Here, the blockage effect becomes very important, so an estimation of its influence on the aerodynamic characteristics requires additional study.

References

- Bossel, H.H., 1971. Vortex computation by the method of weighted residuals using exponentials, *AIAA J.* **9**(9), 2027–2034.
- Carter, J.E., 1979. A new boundary-layer inviscid iteration technique for separated flow, AIAA Paper No. 79-1450.
- Cebeci, T., and Smith, A.M.O., 1974. *Analysis of Turbulent Boundary Layers*, Academic Press, New York.
- Cross, A.G.T., 1986. Boundary-layer calculation and viscous–inviscid coupling, ICAS-86-2.4.1.
- Dvorak, F.A., and Woodward, F.A., 1977. A viscous potential flow interaction analysis method for multi-element infinite swept wing, NASA CR-2476, 1.
- Green, J.E., Weeks, D.W., and Brooman, J.W.F., 1977. Prediction of turbulent boundary layers and wakes in compressible flow by a lag entrainment method, ARC R&M, No. 3791.
- Haase, W., Stock, H.-W., and Echtle, H., 1987. Computation results for some test cases of viscous transonic flow around airfoils, AIAA Paper No. 87-0422.
- Harris, C.D., 1981. Two-dimensional aerodynamic characteristics of the NACA 0012 airfoil in the Langley 8-foot transonic pressure tunnel, NASA TM-81927.
- Holst, T.L., 1987. Viscous transonic airfoil workshop compendium of results, AIAA Paper No. 87-1460.
- Le Balleur, J.C., 1981. Calcul par couplage fort des écoulements visqueux transsoniques incluant sillages et décollements. Profils d'ailes portants, *Rech. Aerospat.* **3**, 161–185.
- Lifshitz, Yu.B., and Shagaev, A.A., 1988. A mesh-projection scheme for computing transonic flow past an airfoil, *USSR Comput. Maths. Math. Phys.* **28**(4), 134–142.
- Lifshitz, Yu.B., and Shagaev, A.A., 1989. Potential models of transonic flows, *Soviet Phys. Dokl.* **34**(2), 81–83.
- Lighthill, M.J., 1958. On displacement thickness, *J. Fluid Mech.* **4**(4), 383–392.
- Lock, R.C., 1986. Velocity profiles for two-dimensional turbulent separated flows, *Proc. Internat. Conf. on Aerodynamics at Low Reynolds Numbers*, London, Oct. 16–17, 1986.
- Maksymiuk, C.M., and Pulliam, T.H., 1987. Viscous transonic airfoil workshop results using ARC2D, AIAA Paper No. 87-0415.

- Melnik, R., Chow, R., and Mead, H., 1977. Theory of viscous transonic flow over airfoils at high Reynolds number, AIAA Paper No. 77-680.
- Melnik, R., Brook, J., and Mead, H., 1987. GRUMFOIL: A computer code for the computation of viscous transonic flow over airfoils, AIAA Paper No. 87-0414.
- Nieuwland, G.I., 1967. Transonic potential flow around a family of quasi-elliptical aerofoil sections, NLR T-172.
- Theodorsen, T., and Garrick, J.E., 1933. General potential theory of arbitrary wing sections, NACA TR No. 452.
- Thomas, J.L., 1984. Integral boundary-layer models for turbulent separated flows, AIAA Paper No. 84-1615.
- Velichko, S.A., 1990. A solution to the problem of flow over an airfoil at large Reynolds numbers, *Izv. Akad. Nauk SSSR Mekh. Zhidk. Gaza* **4**, 189 (in Russian).
- Velichko, S.A., and Lifshitz, Yu.B., 1990. Computation of attached flow past an airfoil at high Reynolds numbers, *PMM USSR* **54**(3), 359–365.
- Whitcomb, R.T., 1974. Review of NASA supercritical airfoils, ICAS Paper No. 74-10.